ACS APPLIED NANO MATERIALS

www.acsanm.org Article

Refined Tin Nanoparticles by Oxidation−Reduction Treatment for Use in Potassium-Ion Batteries

Meng Yu,[‖] Lie Yang,[‖] Liuyang Sun, Yongqiang Zhang, R. Narayan, Yuanbin Qin, Qinqin Fu, Liqiang Zhang, and Xiaohui Ning*

Cite This: *ACS Appl. Nano Mater.* 2021, 4, 4432−4440 Read Online

ACCESS | Metrics & More | Article Recommendations | Supporting Information

ABSTRACT: A unique method is developed to synthesize Sn nanomaterials. Through an oxidation−reduction treatment, Sn particles are refined from the submicron (300 nm) to nanoscale (88 nm). With a series of *ex situ* and *in situ* experiments, we confirm that the Sn refinement follows the scattered nucleation and restricted fusion mechanism. The carbon films forming in oxidation play a key role in inducing the refinement as they restrict the agglomeration of Sn nanoparticles to keep the narrow size distribution. When used as anodes for potassium-ion batteries, the obtained Sn nanoparticles restricted in carbon films (r-Sn/C) exhibit enhanced cycling stability and capacity retention. This unprecedented treatment provides some enlightenment to produce functional nanomaterials used for energy storage applications.

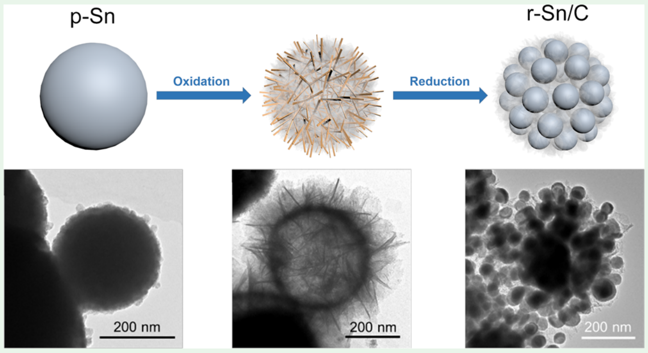

KEYWORDS: *nanomaterials, refining, tin, potassium-ion battery, oxidation, reduction*

1. INTRODUCTION

The ever-growing demand of portable devices, electric vehicles, and large-scale energy storages calls for high-energy-density and low-cost batteries.[1−3] Despite a wide range of applications, lithium-ion batteries can hardly satisfy the low-cost requirement for its scarcity and uneven distribution in the earth crust.[4,5] This has imposed extensive research on sodium-ion and potassium-ion batteries, as both sodium and potassium have abundant resources, low cost, and similar nature to lithium.[6,7] Moreover, potassium (−2.93 V *vs* Li/Li$^+$) shows a lower standard potential than sodium (−2.71 V *vs* Li/Li$^+$), making it able to achieve a higher energy density.[8] In this scenario, the potassium-ion battery can be regarded as a promising alternative to the lithium-ion battery.

As an alloy-type anode, Sn has been prevalent in lithium-ion and sodium-ion batteries for its high theoretical capacity of 991 and 845 mA h g^{-1}, respectively.[9−14] Furthermore, Sn can also form multiple alloys with potassium, showing great potential in potassium-ion batteries. Glushenkov et al. reported a Sn-based anode for the first time to be used in potassium-ion batteries.[15] Unfortunately, the large K-ion radius (1.38 Å) causes severe volume changes and sluggish kinetics upon charge−discharge cycles, greatly restricting the electrochemical activity of Sn.[16]

Nanotechnology seems to be the ideal choice to address this issue. Owing to the unique size and surface effect, nano Sn is supposed to show accelerated kinetics, shortened distance, enhanced reaction activity, and constrained volume expansion toward K ions.[17−21] Thus far, one versatile approach, ball milling, has been developed to synthesize Sn nanomaterials used in potassium-ion batteries. A variety of Sn-based products, such as Sn−C, Sn−Sb, and Sn_4P_3/C, have been fabricated to achieve favorable electrochemical properties.[15,22−26] As a typical method to obtain nanomaterials, ball milling is superior to other methods (hydrothermal process, sol−gel reaction, etc.) for its simplicity to obtain high-purity products and fabricate massive nanomaterials.[27−30] However, the agglomeration and uneven size distribution caused by ball milling severely impair the K-ion storage performance in Sn-based anodes. The introduction of carbon materials, such as graphene and amorphous carbon, has been prevalent to constrain the growth and agglomeration of metals or metal oxides.[31−37] We previously used glucose-derived carbon films to successfully limit the growth and agglomeration of SnO_2 nanosheets, with the obtained SnO_2/C exhibiting enhanced lithium storage performance.[38]

Herein, we used a unique oxidation−reduction method to process pristine Sn (p-Sn) at the submicron scale. Glucose, a cheap and environmentally benign carbon source, is chosen to be hydrothermally oxidized with p-Sn to acquire SnO_2

Received: December 31, 2020
Accepted: April 21, 2021
Published: May 4, 2021

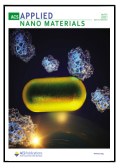

nanosheets that disperse in amorphous carbon films (this intermediate product is denoted as SnO_2/C). Furthermore, reducing SnO_2/C with H_2 harvests Sn nanoparticles well scattered in carbon films (the final product is named r-Sn/C). The introduction of the glucose-derived carbon films through the oxidation−reduction method is aimed at restricting the growth and agglomeration of Sn to achieve the refinement from the submicron to nanoscale. With a series of *ex situ* and *in situ* experiments, we found that the refinement of Sn undergoes scattered nucleation and restricted fusion. The carbon films, formed as a result of the decomposition of glucose, were confirmed to be indispensable for the refinement. Benefiting from the unique nanostructure, r-Sn/C exhibits enhanced electrochemical activity toward K-ion storage. As an anode for potassium-ion batteries, r-Sn/C delivers a reversible capacity of 211.9 mA h g^{-1} after 200 cycles at 0.1 A·g^{-1} and 101.1 mA h g^{-1} over 180 cycles at 1 A·g^{-1}. A discharge capacity of 95.6 mA h g^{-1} can even be achieved at a higher rate of 2 A·g^{-1}. We believe that this unprecedented oxidation−reduction method provides a guideline for synthesizing functional nanomaterials used for novel energy storage.

2. EXPERIMENTAL SECTION

2.1. Synthesis of p-Sn. p-Sn was prepared by the reduction of $SnCl_2$ (Aladdin) with $NaBH_4$ (Aladdin), as was reported in our previous work.[38]

2.2. Preparation of the SnO_2/C Intermediate. The SnO_2/C intermediate was synthesized by a hydrothermal oxidation process described as follows. First, both 0.3 g of the as-acquired p-Sn and glucose (Aladdin) were added in 60 mL of deionized water with ultrasonic treatment for 30 min. Then, the mixture was transferred into a 100 mL Teflon-lined stainless-steel autoclave and subsequently put in an oven with heating at 180 °C for 20 h. After cooling to the ambient temperature, the products were centrifuged by using deionized water and ethanol several times and dried at 80 °C overnight. Finally, the chestnut-like SnO_2/C intermediate was obtained.

2.3. Synthesis of r-Sn/C. r-Sn/C was obtained through the reduction of SnO_2/C under a H_2 atmosphere. Typically, the intermediate was put into a tube furnace and heated at 450 °C. During annealing, 270 sccm Ar mixed with 30 sccm H_2 was continuously introduced into the furnace. The reduction process was carried out for 30 min. After cooling down to room temperature, r-Sn/C was acquired.

2.4. Material Characterization. The micromorphology of the synthesized samples was characterized by using a field-emission scanning electron microscope (Hitachi SU6600). The inner structure and element distribution were investigated by using a high-resolution transmission electron microscope (HRTEM, JEOL 2100, 200 kV) equipped with an energy-dispersive X-ray spectrometer. The internal morphology was also observed by using a scanning electron microscope combined with focused ion beam (SEM/FIB, Helios NanoLab DualBeam). The crystal structure was examined by X-ray diffraction (XRD, PANalytical X'pert Pro, Cu: 40 kV, 40 mA). The carbon content was analyzed by thermogravimetry (TG, METTLER TOLEDO, O_2, 35−650 °C).

2.5. *In Situ* TEM Study on the Reduction Process. The *in situ* TEM technique was employed to observe the real-time reduction process. The experiment was conducted on a Cs-corrected ETEM instrument (FEI, Titan G2, 300 kV) by placing the sample on a FEI-NanoEx-i/v holder. High-purity H_2 (99.99%) was introduced in the specimen chamber with the pressure controlled at 1.0 mbar. The reduction experiment was conducted at different temperatures, and the morphological response of SnO_2/C during heating was recorded for further detailed analysis.

2.6. Electrochemical Measurements. p-Sn or r-Sn/C was further treated to be the negative electrode. First, the sample was mixed with super-P carbon and polyvinylidene fluoride binder (8:1:1 in mass ratio) in *N*-methyl pyrrolidone solvent under vigorous agitation of 24 h. The slurry obtained was then cast onto copper foil and dried overnight at 80 °C under vacuum. Next, the electrode was cut into several discs with a diameter of 12 mm and a mass loading of 1.0 mg·cm^{-2}. For the counter electrode, bulk metal potassium was treated to be potassium wafers with a diameter of 16 mm. After preparing both electrodes, we assembled CR2032-type coin cells in an Ar-filled glovebox (Unilab, MBraun) by employing a potassium wafer as the counter electrode, a glass microfiber filter (Whatman, GF/D) as the separator, and 1 M KFSI in ethylene carbonate/diethyl carbonate (1:1 by volume) as the electrolyte. The O_2 and H_2O concentrations in the glovebox were maintained below 0.1 ppm. The electrochemical properties were tested on a battery tester (BST8-MA, MTI) and an electrochemical workstation (CHI660E, Shanghai Chenhua).

3. RESULTS AND DISCUSSION

3.1. Investigation of Products. The synthesis of r-Sn/C includes two steps, schematically depicted in Figure 1a. First, p-Sn was oxidized in glucose solution to form chestnut-like SnO_2/C via a hydrothermal reaction. Oxygen in air and in H_2O acted as the oxidizing agent, while glucose decomposed to generate carbon. Second, SnO_2/C was thermally reduced with H_2 to generate r-Sn/C. According to the TG curve

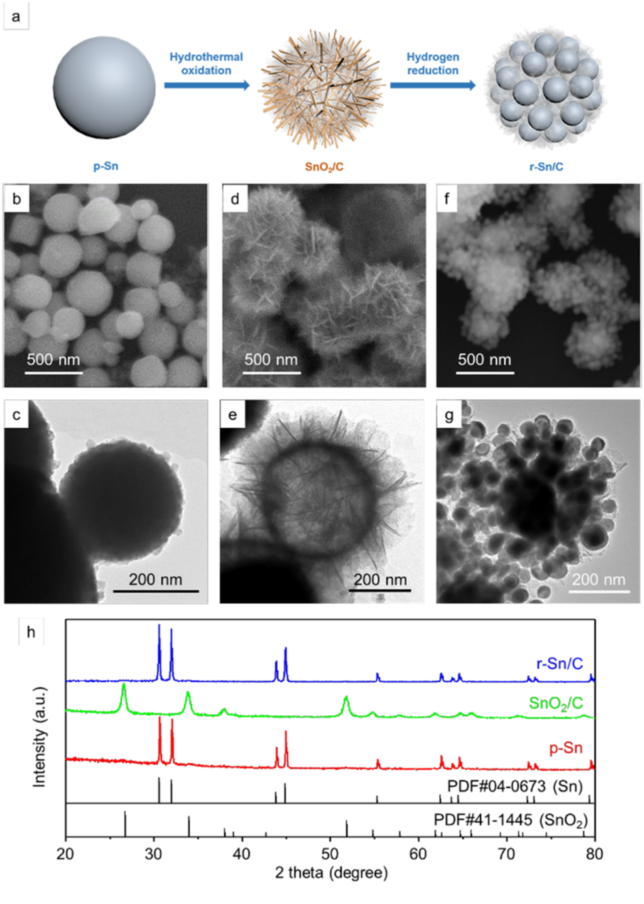

Figure 1. Morphological and structural characterization of products. (a) Schematic of the "oxidation−reduction" process, from p-Sn to SnO_2/C and then to r-Sn/C; (b) SEM and (c) TEM images of p-Sn; (d) SEM and (e) TEM images of SnO_2/C; (f) SEM and (g) TEM images of r-Sn/C; and (h) XRD patterns of p-Sn, SnO_2/C and r-Sn/C.

displayed in Figure S1, the carbon content in r-Sn/C is calculated as 32.2 wt %.

We first investigated the evolution from p-Sn to r-Sn/C through a series of *ex situ* techniques. SEM images of p-Sn, SnO_2/C and r-Sn/C are, respectively, shown in Figure 1b,d,f, while their corresponding TEM images are depicted in Figure 1c,e,g. p-Sn is seen to contain a lot of spherical solid particles with a diameter more than 200 nm. After oxidation, each big particle was split into a hollow chestnut sphere, which consists of numerous SnO_2 nanosheets supported by carbonaceous films. TEM images at various tilt angles in Figure S2a show that these lathy nanosheets are randomly dispersed in the substance. From the high-resolution TEM image in Figure S2b, this substance shows an amorphous structure as indicated by the black arrows. The amorphous substance originates from the decomposition of glucose during oxidation. With further reduction, SnO_2 nanosheets were converted to spherical solid Sn nanoparticles scattered in the amorphous films. Compared with p-Sn, r-Sn/C shows a vastly decreased size and inherits the spherical solid structure. XRD patterns of p-Sn, SnO_2/C, and r-Sn/C are displayed in Figure 1h. p-Sn and r-Sn/C conforms perfectly to the tetragonal structure of Sn with the *amd*(141) group (JCPDS # 04-0763), while SnO_2/C can be indexed to the tetragonal structure of SnO_2 with the *mnm*(136) group (JCPDS # 41-1445). XRD results confirm the structural transition from Sn to SnO_2 and then back to Sn. No signals of other structures further indicate the amorphous nature of the films in SnO_2/C and r-Sn/C. These *ex situ* techniques of SEM, TEM, and XRD give an overall insight into the morphology and structure of the three products obtained.

More details were given on r-Sn/C with the results shown in Figure 2. The enlarged TEM images of r-Sn/C are displayed in Figure 2a,b. Spherical solid Sn nanoparticles are clearly seen to be scattered in the consecutive films indicated by the black arrow. The insets in Figure 2b reveal the (200) crystal face of tetragonal Sn (JCPDS # 04-0763) with 2.95 Å lattice spacing. Moreover, these refined Sn nanoparticles have a diameter below 100 nm, real nanomaterials. We further measured more than 200 particles of either p-Sn or r-Sn/C and confirmed the average diameters to be 300 and 88 nm, respectively. The size distribution of both samples is schematically shown in Figure 2c, where a narrower size distribution of r-Sn/C can be found. Figure 2d depicts the EDS mapping of r-Sn/C, confirming the only two elements of C and Sn. These detailed analyses of r-Sn/C unveil the unique structure of Sn nanoparticles, which are well scattered within the carbon films and have narrow size distribution.

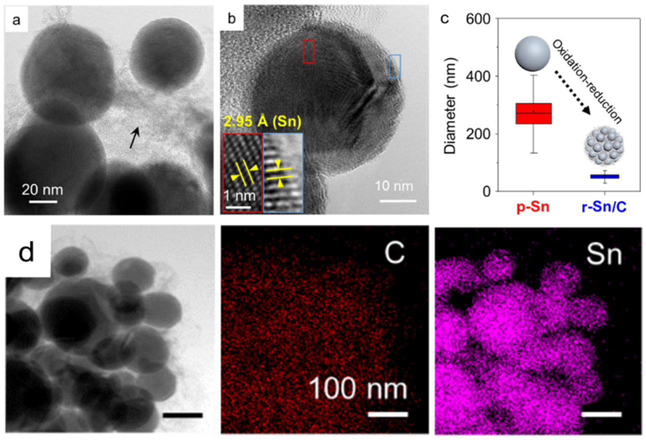

Figure 2. Detailed characterization of r-Sn/C. (a) Magnified TEM image; (b) magnified TEM image of an individual nanoparticle with the high-resolution TEM images in the insets; (c) size distribution of p-Sn and r-Sn/C; and (d) EDS mapping results of two elements: C and Sn. All scale bars in d are 100 nm.

Through the oxidation−reduction treatment, spherical solid Sn particles were refined from 300 to 88 nm. In order to have a comprehensive and in-depth knowledge of the refinement, we focused on the individual step of either oxidation or reduction and conducted a series of *ex situ* and *in situ* experiments.

3.2. Refinement Mechanism. In order to investigate the evolution of the oxidation process, we synthesized a series of products by controlling the oxidative time to 0, 3, 5, and 20 h. The cross-sectional SEM images of these products are shown in Figure 3a−d. All of these images are obtained using the FIB technique. Before oxidation (0 h), p-Sn has a spherical solid structure; with oxidation proceeding (3 h), a lot of voids emerge beneath the shell and the core@void@shell structure comes to being; as the oxidation goes on further (5 h), these voids grow larger at the expense of the core shrinking, with the formation of a small core@large void@shell structure; after oxidation (20 h), a complete hollow structure forms. Our previous work has confirmed the gradual transition from Sn to SnO_x (SnO/SnO_2) and then to complete SnO_2 under oxidation.[38] Furthermore, some burrs come to bestrew the shell after oxidation of 5 h and grow further until the formation of the hollow structure. The core-shrinking and surface-roughening process is schematically illustrated in Figure 3e. We suppose that the outward diffusion rate of Sn is larger than the inward of O, leading to a gradual expansion of the voids. This characteristic phenomenon should be ascribed to the Kirkendall effect, a famous phenomenon used for preparing hollow nanomaterials.[39,40] Through this phenomenon, internal Sn diffuses onto the surface and is oxidized to form SnO_2. Moreover, promoted by glucose-induced decomposition, SnO_2 grows preferentially along the [110] direction to form the randomly scattered nanosheets into the amorphous carbon films.[38] These SnO_2 nanosheets combine with the carbon films to constitute the chestnut-like SnO_2/C intermediate, which serves as the template for obtaining r-Sn/C.

We further studied the reduction of SnO_2/C to r-Sn/C by adjusting the H_2 flow rate to 0, 15, and 30 sccm to obtain a series of products. Their XRD patterns are shown in Figure S3. Without H_2, SnO_2/C cannot be reduced because only the characteristic SnO_2 diffraction peaks (JCPDS # 41-1445) are found; with 15 sccm H_2, the typical diffraction peaks of SnO_2 (JCPDS # 41-1445), SnO (JCPDS # 06-0395), and Sn (JCPDS # 04-0763) are observed; with 30 sccm H_2, only the Sn diffraction peaks (JCPDS # 04-0763) can be seen. These XRD results confirm the gradual reduction process with SnO as the intermediate. Characteristic C diffraction peaks are not found in all samples due to the amorphous nature of the carbon films. For distinction, we name the products after 0 H_2, 15 sccm H_2, and 30 sccm H_2 SnO_2/C, SnO_x/C, and Sn, respectively. Figure 4a−c displays the respective TEM images of SnO_2/C, SnO_x/C, and Sn, with their magnified TEM images shown in Figure 4d−f. The insets are the respective HRTEM images. Before reduction, SnO_2/C has a hollow and chestnut-like structure (Figure 4a). The magnified and high-resolution images (Figure 4d and the inset) confirm the (110) crystal face of tetragonal SnO_2 (JCPDS # 41-1445) with 3.38 Å lattice spacing. With reduction proceeding, Sn signals come to

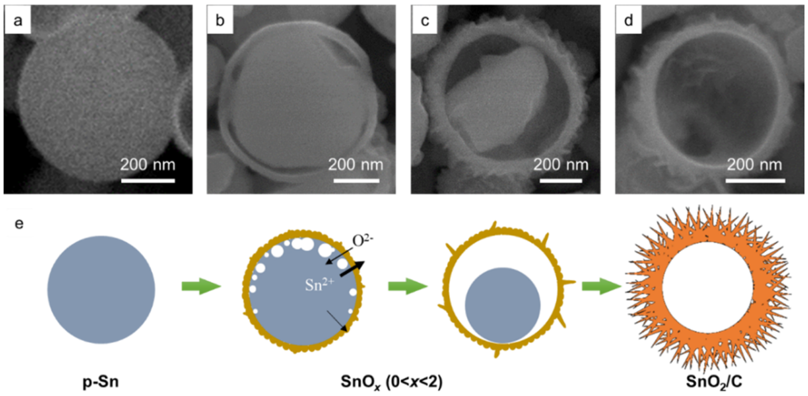

Figure 3. Oxidation of p-Sn. (a−d) Cross-sectional SEM images of the oxidation products obtained at different oxidative times: (a) 0 h (Sn), (b) 3 h (SnO_x), (c) 5 h (SnO_x), and (d) 20 h (SnO_2). These cross sections were created via FIB and (e) schematic of the structural evolution process.

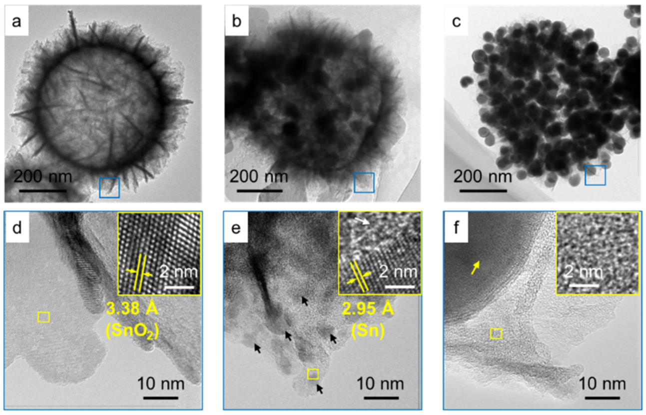

Figure 4. Reduction of SnO_2/C. TEM images of (a) SnO_2/C, (b) SnO_x/C, and (c) r-Sn/C; (d−f) corresponding magnified TEM images of the blue areas in (a−c). The insets are high-resolution TEM images of the corresponding yellow areas.

emerge (Figure 4b). According to the magnified image (Figure 4e), the protruding SnO_2 nanosheet (dark area) gradually disappears and some Sn nuclei come into being, as indicated by the black arrows. The inset shows that these nuclei belong to the tetragonal Sn (JCPDS # 04-0763) with the 2.95 Å lattice spacing corresponding to the (200) crystal face. Note that these Sn nuclei are scattered and isolated by the amorphous carbon films indicated with the white arrow. On sufficient reduction, Sn nanoparticles dispersed in carbon films form (Figure 4c). From the magnified image (Figure 4f), the Sn nuclei move to fuse into a nanoparticle, as indicated by the yellow arrow. Moreover, the inset confirms the amorphous film around the nanoparticle. These results reveal the scattered nucleation of Sn nanoparticles.

We suppose that the carbon films play an important role in restricting the growth of Sn nanoparticles. To validate this, we removed the carbon in SnO_2/C beforehand by calcining it in air to obtain SnO_2. The SEM images of Sn reduced from SnO_2/C and SnO_2 are respectively shown in Figure S4a,b. Enormous well-dispersed Sn nanoparticles are obtained from reducing SnO_2/C, whereas the reduction of SnO_2 can only attain agglomerated Sn particles. Therefore, the refinement of Sn cannot be achieved without the carbon films. We further validate the stability of the carbon films at high temperature and in the long term. With the reduction temperature increasing from 500 (Figure S4c) to 650 °C (Figure S4d) and then to 800 °C (Figure S4e) or the time lengthening from 0.5 (Figure S4f) to 2 h (Figure S4g) and then to 4 h (Figure S4h), the carbon films stay considerably stable and disperse Sn nanoparticles well through.

We employed a series of *ex situ* experiments to verify the scattered nucleation of Sn nanoparticles and the indispensable role of the carbon films. However, more direct and intuitional evidence is required. The *in situ* technique was therefore introduced. Herein, we placed SnO_2/C onto an environmental transmission electron microscope, where H_2 can be filled and

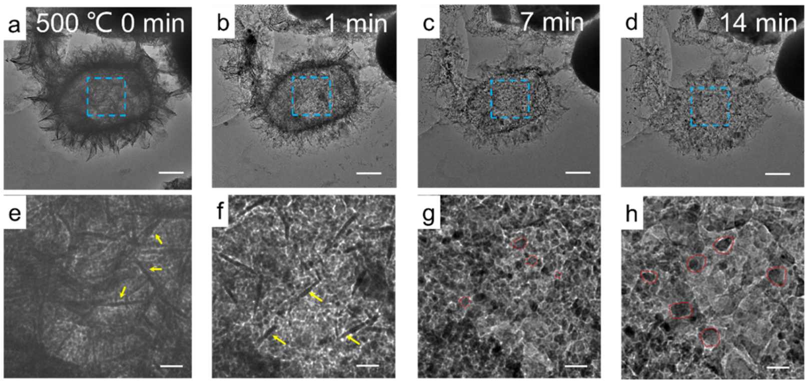

Figure 5. TEM Snapshots taken from the *in situ* reduction of SnO_2/C. TEM images taken at (a) 0, (b) 1, (c) 7, and (d) 14 min; (e−h) corresponding magnified TEM images of the blue-dash areas in (a−d). The *in situ* process is conducted at 500 °C in 1 mbar H_2. The scale bar is 100 nm in (a−d) and 20 nm in (e−h).

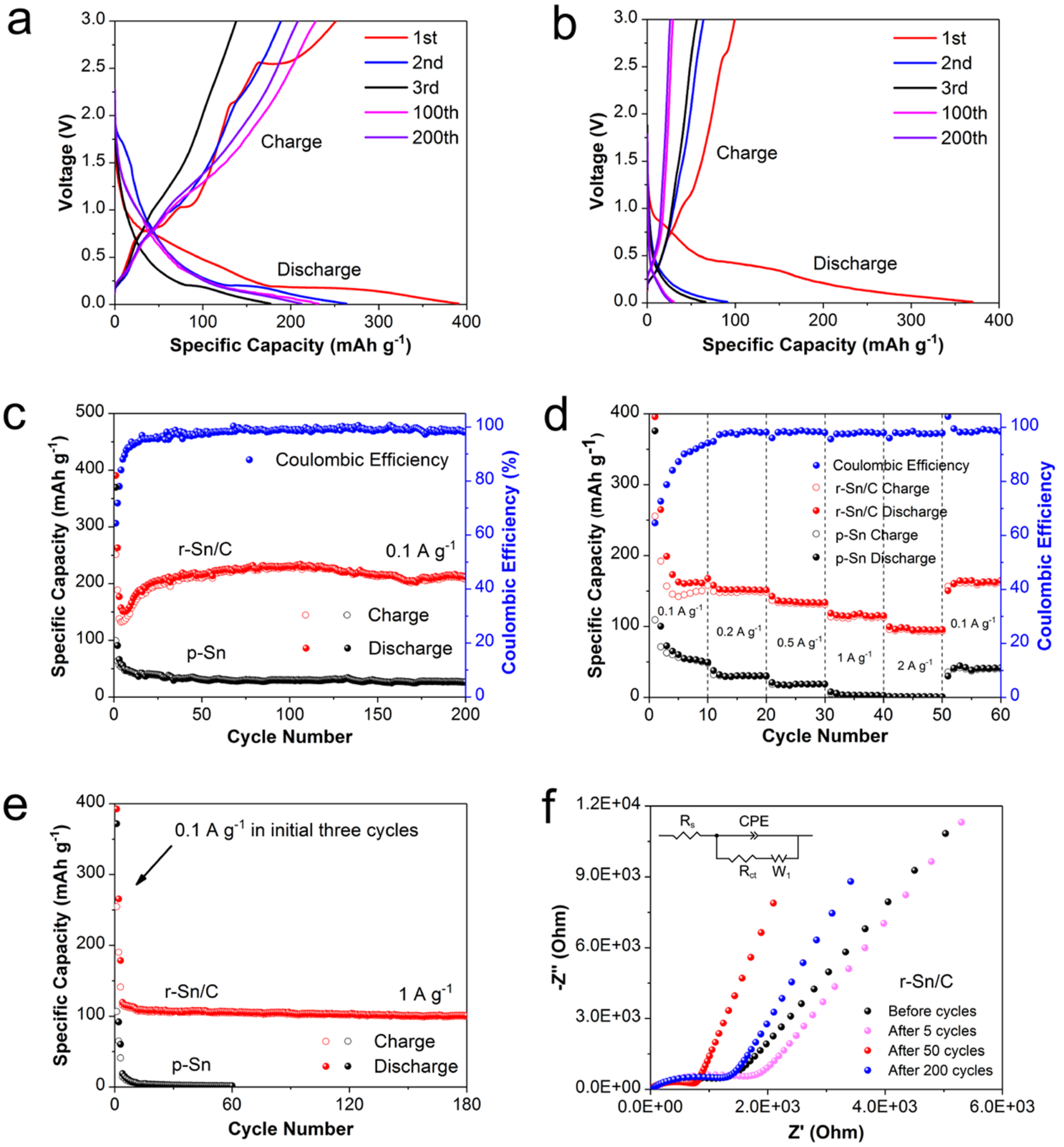

Figure 6. Potassium-ion storage properties of r-Sn/C and p-Sn. Galvanostatic charge−discharge curves of (a) r-Sn/C and (b) p-Sn in selected cycles tested at 0.1 A g^{-1}; (c) cycling performance of r-Sn/C and p-Sn at a current density of 0.1 A g^{-1}, with the Coulombic efficiency of r-Sn/C shown; (d) rate properties of r-Sn/C and p-Sn tested at different current densities, with the Coulombic efficiency of r-Sn/C displayed; (e) cycling performance of r-Sn/C and p-Sn at a high rate of 1 A g^{-1}, with both samples cycled at 0.1 A g^{-1} in initial three cycles; and (f) Nyquist plots of r-Sn/C obtained at 5 mV between 0.1 and 10^5 Hz before or after cycles at 0.1 A g^{-1}, with the equivalent circuit shown in the inset.

temperature can be controlled to induce the reduction. The dynamic evolution of SnO_2/C at different temperatures is shown in Movie S1 and Movie S2. As seen in Movie S1, SnO_2/C shows no change in its structure below 400 °C, suggesting that it cannot be reduced at low temperature. When the temperature increases to 500 °C (Movie S2), the structure evolves gradually from SnO_2/C to r-Sn/C. Some snapshots from Movie S2 were taken for studying the real-time reduction. Those taken at 0, 1, 7, and 14 min are respectively displayed in Figure 5a−d, where the corresponding blue-dash areas are further shown in Figure 5e−h. With the reduction proceeding, the lathy nanosheets (indicated by the yellow arrows) gradually disappear while some Sn nuclei come to emerge (indicated by the red-dash cycles). As the reduction goes on further, these nuclei move and fuse to form larger particles. The carbon films provide a viable path for the motion and integration of Sn nuclei, but it also restricts the large-scale fusion and agglomeration of Sn. Through this *in situ* observation, we gained an insight into the formation of r-Sn/C, which includes not only the scattered nucleation but also the restricted fusion, as illustrated in Figure S5.

Through these *ex situ* and *in situ* experiments, we gained a comprehensive knowledge of the Sn refinement, which can be summarized as follows. The refinement is achieved by an oxidation−reduction process. During oxidation, glucose decomposes to induce the oriented growth of SnO_2 nanosheets with the generated carbon films to form the hollow chestnut-like SnO_2/C; during reduction, the carbon films restrict the excess fusion of Sn to generate r-Sn/C.

3.3. Potassium-Ion Storage Properties. To validate the application potentiality of r-Sn/C, we further evaluated its electrochemical behavior as anode materials for potassium-ion batteries with p-Sn as a comparison. Cells were tested at various rates within 0.01−3 V. Figure 6a,b shows the galvanostatic charge−discharge curves of r-Sn/C and p-Sn at 0.1 A g^{-1}, respectively. r-Sn/C is seen to show a long 1st discharge plateau below 0.25 V, delivering a high capacity of 390.6 mA h g^{-1}. However, its 1st charge capacity retains only 251.2 mA h g^{-1}, with a Coulombic efficiency of 64.3%. The large capacity loss should be ascribed to the irreversible interfacial reactions that consume massive potassium ions to form a solid electrolyte interface (SEI).[15] Several short plateaus are found in the first charge curve, which can be ascribed to the multiphase dealloying reactions.[28] The charge and discharge plateaus in the subsequent cycles become unobvious, indicating the weakened electrochemical activity after the first cycle. The cyclic voltammetry curves of r-Sn/C were further measured to investigate the electrochemical reactions, with the results shown in Figure S6, where the multiphase alloying and dealloying reactions between K and Sn are confirmed within 0.1−2.75 V. With respect to p-Sn, more unapparent charge and discharge plateaus can be observed in the first cycle. It delivers an initial charge−discharge capacity of 99.3/369.7 mA h g^{-1} with a Coulombic efficiency as low as 26.9%. The capacity drops fast after the 1st cycle. These galvanostatic charge−discharge curves reveal the enhanced electrochemical activity of r-Sn/C with decent capacity retention during cycles.

The corresponding cycling plots of r-Sn/C and p-Sn at 0.1 A g^{-1} are shown in Figure 6c. As seen, the capacity of r-Sn/C decays fast in the first five cycles and then rises gradually until the 100th cycle, after which it fluctuates slightly with an ultimate discharge capacity of 211.9 mA h g^{-1} after 200 cycles. The cycling stability of r-Sn/C outperforms that of the Sn-based materials reported previously, as seen in Table 1.[15,27,28,41−43] The capacity decay in the initial cycles is attributed to the irreversible side reactions with the formation of the SEI film; the capacity recovery can be ascribed to the activation of Sn nanomaterials after the initial several cycles, which is prevalent in potassium-ion batteries.[15,26−29,41] The Coulombic efficiency of r-Sn/C increases predominantly from 64.3 to 88.1% in the initial five cycles, indicating the gradually decreased side reactions upon cycles. After 50 cycles, r-Sn/C achieves the favorable reversible capacity retention as the Coulombic efficiency reaches up to 99%. On the other hand, the capacity of p-Sn decays sharply below 50 mA h g^{-1} within the first several cycles and maintains at 30.6 mA h g^{-1} over 200 cycles. The highly improved cycling stability of r-Sn/C should be ascribed to its unique structure: first, downsizing Sn particles from the submicron to nanoscale improves the electrochemical activity of r-Sn/C toward K-ion storage, enabling r-Sn/C to deliver more capacities; second, the carbon films play a key role in mitigating the agglomeration and pulverization of Sn nanoparticles upon cycles to maintain the structural stability of r-Sn/C. The electrochemical properties of SnO_2/C in potassium-ion batteries were also investigated, with the results depicted in Figure S7. It can be found that the cycling stability and capacity retention of SnO_2/C are better than those of p-Sn while inferior to those of r-Sn/C. This result further confirms the significant role of the carbon films in improving the cycling performance of Sn-based materials.

Table 1. Comparison of Cycling Performance between r-Sn/C and Sn-Based Materials Reported Previously

materials	rate (A g^{-1})	cycle numbers	capacity (mA h g^{-1})	literature
Sn−MoS_2/C	0.1	50	239	27
Sn/NPC	0.05	200	198	41
SnO	0.025	30	183	42
Sn−C	0.025	30	110	15
3D-HPCS	0.05	100	276.4	28
Sn@RGO	0.1	50	200	43
r-**Sn/C**	**0.1**	**200**	**211.9**	**this work**

We further evaluated the electrochemical behavior of p-Sn and r-Sn/C at higher rates, with the results shown in Figure 6d. The capacity of both samples declines with the rate increasing from 0.1 to 2 A g^{-1}. When it returns back to 0.1 A g^{-1}, the capacity can recover to the initial level. The capacity decay is due to the severe polarization at high rates; the capacity recovery indicates the favorable electrochemical reversibility of both samples. In addition, the Coulombic efficiency of r-Sn/C in the initial 10 cycles stays below 95%, suggesting the severe interfacial reactions at the rate of 0.1 A g^{-1}. After 10 cycles, the capacity of r-Sn/C at every rate becomes stabilized with higher Coulombic efficiency above 98%. It should be noted that at 11th, 21st, 31st, 41st, and 51st cycles, the Coulombic efficiency drops or rises drastically, which can be put down to the variation of the current density that impacts the polarization of r-Sn/C thus causing remarkable changes between charge and discharge capacities. At the rate of 0.1, 0.2, 0.5, 1.0, and 2.0 A g^{-1}, r-Sn/C delivers capacities of 167.8 (10th), 151.5 (20th), 133.8 (30th), 115.4 (40th), and 95.6 mA h g^{-1} (50th), respectively, while p-Sn shows capacities of only 49.7 (10th), 30.4 (20th), 18.8 (30th), 2.9 (40th), and 1.0 mA h g^{-1} (50th), respectively. Even at high rates of 1.0 and 2.0 A g^{-1}, r-Sn/C exhibits decent capacity retention, whereas p-Sn can hardly deliver capacity. The long cyclic stability of the two samples was further evaluated at 1 A g^{-1}. The cells were activated at 0.1 A g^{-1} in initial three cycles. As shown in Figure 6e, the discharge capacity of r-Sn/C drops quickly in the initial three cycles at 0.1 A g^{-1}, from 392.7 to 178.5 mA h g^{-1}. This result is consistent with the results in Figure 6c,d. The massive capacity loss in these initial cycles can be attributed to the irreversible interfacial reactions with the formation of the SEI. After the activation process, a capacity attenuation is still observed from 4th to 11th cycles, with the discharge capacity declining to 110.6 mA h g^{-1}. This indicates the side reactions still remain but decrease drastically. In the later cycles, r-Sn/C undergoes a gradual capacity fade with slight capacity fluctuation, delivering a stabilized capacity of 101.1 mA h g^{-1} after 180 cycles. As for p-Sn, however, the discharge capacity drops sharply below 5 mA h g^{-1} after 12 cycles. As a consequence, the superiority of r-Sn/C toward potassium-ion storage becomes more obvious at higher rates, where p-Sn shows little electrochemical activity to potassium ions.

According to the above results, we suppose the favorable cycling stability and capacity retention of r-Sn/C to be concerned with its kinetics; EIS measurement of r-Sn/C was therefore implemented with p-Sn as a comparison. Cells were tested at 5 mV between 0.01 and 10^5 Hz before or after cycles at 0.1 A g^{-1}. The Nyquist plots of r-Sn/C and p-Sn are displayed in Figures 6f and S8 with the equivalent circuits shown in the inset. The semicircles in medium-high frequencies reflect the charge transfer impedance (R_{ct}) while the straight lines in low frequencies represent the Warburg impedances involved in the diffusion of K ions into the electrode materials. The R_{ct} and the diffusion coefficient of K ions (D_K) were calculated on the basis of Figures 6f, S8, and

S9, with the results displayed in Table S1. It can be found that r-Sn/C, compared with p-Sn, exhibits declined R_{ct} and enhanced D_K upon cycles; moreover, r-Sn/C shows the optimal values of R_{ct} and D_K at the 50th cycle. The kinetics are predominantly accelerated from the 5th cycle to the 50th cycle. The enhanced kinetics are favorable for reducing the polarization of r-Sn/C to induce a capacity activation process during the cycles, which is in accordance with the results shown in Figure 6c. On the other hand, the sluggish kinetics of p-Sn are aggravated with the cycles as a result of the increased R_{ct} and the declined D_K, leading to a continuous capacity attenuation of p-Sn. These EIS results of r-Sn/C and p-Sn are consistent with their galvanostatic charge−discharge results.

4. CONCLUSIONS

In summary, we developed a facile oxidation−reduction method to achieve the refinement of Sn particles from the submicron to nanoscale. Through a series of *ex situ* and *in situ* experiments, we validate that the refinement undergoes the scattered nucleation and restricted fusion of Sn. The carbon films, generated by the decomposition of glucose, act as indispensable for inducing the growth of Sn while limiting its further agglomeration. Benefiting from the refined nanosize and the restriction of carbon films, r-Sn/C exhibits remarkably enhanced electrochemical properties when used as anodes for potassium-ion batteries. We believe this unprecedented process can serve as a guideline for synthesizing functional nanomaterials employed in energy storage.

■ ASSOCIATED CONTENT

Supporting Information

The Supporting Information is available free of charge at https://pubs.acs.org/doi/10.1021/acsanm.0c03475.

TG curve of r-Sn/C; TEM images; XRD patterns; SEM images; schematic of the scattered nucleation and restricted fusion; CV curves; galvanostatic charge−discharge curves; fitting lines of Z'; and Rct and DK of r-Sn/C and p-Sn (PDF)

SnO_2/C shows no change in its structure below 400 °C (MP4)

Structural change from SnO_2/C to r-Sn/C (MP4)

■ AUTHOR INFORMATION

Corresponding Author

Xiaohui Ning − *Center for Advancing Materials Performance from the Nanoscale (CAMP-Nano), State Key Laboratory for Mechanical Behaviour of Materials School of Materials Science and Engineering, Xi'an Jiaotong University, Xi'an, Shaanxi 710049, P. R. China;* orcid.org/0000-0002-1720-8946; Email: xiaohuining@mail.xjtu.edu.cn

Authors

Meng Yu − *Center for Advancing Materials Performance from the Nanoscale (CAMP-Nano), State Key Laboratory for Mechanical Behaviour of Materials School of Materials Science and Engineering, Xi'an Jiaotong University, Xi'an, Shaanxi 710049, P. R. China*

Lie Yang − *Center for Advancing Materials Performance from the Nanoscale (CAMP-Nano), State Key Laboratory for Mechanical Behaviour of Materials School of Materials Science and Engineering, Xi'an Jiaotong University, Xi'an, Shaanxi 710049, P. R. China;* orcid.org/0000-0002-8455-3272

Liuyang Sun − *Center for Advancing Materials Performance from the Nanoscale (CAMP-Nano), State Key Laboratory for Mechanical Behaviour of Materials School of Materials Science and Engineering, Xi'an Jiaotong University, Xi'an, Shaanxi 710049, P. R. China*

Yongqiang Zhang − *Center for Advancing Materials Performance from the Nanoscale (CAMP-Nano), State Key Laboratory for Mechanical Behaviour of Materials School of Materials Science and Engineering, Xi'an Jiaotong University, Xi'an, Shaanxi 710049, P. R. China;* orcid.org/0000-0002-4192-5961

R. Narayan − *Department of Materials Science and Engineering, Indian Institute of Technology, Delhi, New Delhi 110016, India*

Yuanbin Qin − *Center for Advancing Materials Performance from the Nanoscale (CAMP-Nano), State Key Laboratory for Mechanical Behaviour of Materials School of Materials Science and Engineering, Xi'an Jiaotong University, Xi'an, Shaanxi 710049, P. R. China*

Qinqin Fu − *Center for Advancing Materials Performance from the Nanoscale (CAMP-Nano), State Key Laboratory for Mechanical Behaviour of Materials School of Materials Science and Engineering, Xi'an Jiaotong University, Xi'an, Shaanxi 710049, P. R. China*

Liqiang Zhang − *State Key Laboratory of Heavy Oil Processing, Beijing Key Laboratory of Failure, Corrosion, and Protection of Oil/Gas Facilities, China University of Petroleum Beijing, Beijing 102249, China*

Complete contact information is available at: https://pubs.acs.org/10.1021/acsanm.0c03475

Author Contributions

[‖]M.Y. and L.Y. contributed equally to this work.

Notes

The authors declare no competing financial interest.

■ ACKNOWLEDGMENTS

The authors appreciate the financial support from the National Natural Science Foundation of China (U1766216, 51401157, 51971245), the National Key Research and Development Program of China (no. 2017YFB0702001), Beijing Natural Science Foundation of China-Haidian Special Project (L182065), Beijing Natural Science Foundation of China (2202046), and the State Key Laboratory for Mechanical Behavior of Materials (20192103). The authors also acknowledge the International Joint Laboratory for Micro/Nano Manufacturing and Measurement Technologies for the test service.

■ REFERENCES

(1) Armand, M.; Tarascon, J.-M. Building Better Batteries. *Nature* **2008**, *451*, 652−657.

(2) Hu, Y.; Wu, K.; Zhang, F.; Zhou, H.; Qi, L. Hierarchical MnO@C Hollow Nanospheres for Advanced Lithium-Ion Battery Anodes. *ACS Appl. Nano Mater.* **2019**, *2*, 429−439.

(3) Salman, M. S.; Park, A. R.; Cha, M. J.; Choi, Y.; Jang, S. K.; Tan, L.; Yoo, P. J.; Choe, W.-S. Lysozyme-Templated Meso-Macroporous Hollow TiO_2 for Lithium Ion Battery Anode. *ACS Appl. Nano Mater.* **2018**, *1*, 698−710.

(4) Larcher, D.; Tarascon, J.-M. Towards Greener and More Sustainable Batteries for Electrical Energy Storage. *Nat. Chem.* **2015**, *7*, 19−29.

(5) Liu, M.-C.; Li, J.; Yang, Q.-Q.; Xu, Y.; Kong, L.-B.; Bai, R.-J.; Liu, W.-W.; Niu, W.-J.; Chueh, Y.-L. Hierarchically Interconnected Ni_3S_2 Nanofibers as Binder-Free Electrodes for High-Performance Sodium-Ion Energy-Storage Devices. *ACS Appl. Nano Mater.* **2019**, *2*, 2634−2641.

(6) Xie, X.; Kretschmer, K.; Anasori, B.; Sun, B.; Wang, G.; Gogotsi, Y. Porous $Ti_3C_2T_x$ MXene for Ultrahigh-Rate Sodium-Ion Storage with Long Cycle Life. *ACS Appl. Nano Mater.* **2018**, *1*, 505−511.

(7) Jian, Z.; Luo, W.; Ji, X. Carbon Electrodes for K-Ion Batteries. *J. Am. Chem. Soc.* **2015**, *137*, 11566−11569.

(8) Wang, W.; Zhou, J.; Wang, Z.; Zhao, L.; Li, P.; Yang, Y.; Yang, C.; Huang, H.; Guo, S. Short-Range Order in Mesoporous Carbon Boosts Potassium-Ion Battery Performance. *Adv. Energy Mater.* **2017**, *8*, 1701648.

(9) Idota, Y.; Kubota, T.; Matsufuji, A.; Maekawa, Y.; Miyasaka, T. Tin-Based Amorphous Oxide: A High-Capacity Lithium-Ion-Storage Material. *Science* **1997**, *276*, 1395−1397.

(10) De Juan, L. M. Z.; Maggay, I. V. B.; Nguyen, M. T.; Liu, W.-R.; Yonezawa, T. β-Sn Nanorods with Active (001) Tip Induced LiF-Rich SEI Layer for Stable Anode Material in Lithium Ion Battery. *ACS Appl. Nano Mater.* **2018**, *1*, 3509−3519.

(11) Ma, B.; Luo, J.; Deng, X.; Wu, Z.; Luo, Z.; Wang, X.; Wang, Y. Hollow Silicon-Tin Nanospheres Encapsulated by N-Doped Carbon as Anode Materials for Lithium-Ion Batteries. *ACS Appl. Nano Mater.* **2018**, *1*, 6989−6999.

(12) Obrovac, M. N.; Chevrier, V. L. Alloy Negative Electrodes for Li-Ion Batteries. *Chem. Rev.* **2014**, *114*, 11444−11502.

(13) Xu, Y.; Zhu, Y.; Liu, Y.; Wang, C. Electrochemical Performance of Porous Carbon/Tin Composite Anodes for Sodium-Ion and Lithium-Ion Batteries. *Adv. Energy Mater.* **2013**, *3*, 128−133.

(14) Botas, C.; Carriazo, D.; Singh, G.; Rojo, T. Sn- and SnO_2-Graphene Flexible Foams Suitable as Binder-Free Anodes for Lithium Ion Batteries. *J. Mater. Chem. A* **2015**, *3*, 13402−13410.

(15) Sultana, I.; Ramireddy, T.; Rahman, M. M.; Chen, Y.; Glushenkov, A. M. Tin-Based Composite Anodes for Potassium-Ion Batteries. *Chem. Commun.* **2016**, *52*, 9279−9282.

(16) Wu, X.; Leonard, D. P.; Ji, X. Emerging Non-Aqueous Potassium-Ion Batteries: Challenges and Opportunities. *Chem. Mater.* **2017**, *29*, 5031−5042.

(17) Xu, Y.; Liu, Q.; Zhu, Y.; Liu, Y.; Langrock, A.; Zachariah, M. R.; Wang, C. Uniform Nano-Sn/C Composite Anodes for Lithium Ion Batteries. *Nano Lett.* **2013**, *13*, 470−474.

(18) Ying, H.; Han, W.-Q. Metallic Sn-Based Anode Materials: Application in High-Performance Lithium-Ion and Sodium-Ion Batteries. *Adv. Sci.* **2017**, *4*, 1700298.

(19) Mao, J.; Zhou, T.; Zheng, Y.; Gao, H.; Liu, H. k.; Guo, Z. Two-Dimensional Nanostructures for Sodium-Ion Battery Anodes. *J. Mater. Chem. A* **2018**, *6*, 3284−3303.

(20) Yi, Z.; Han, Q.; Geng, D.; Wu, Y.; Cheng, Y.; Wang, L. One-Pot Chemical Route for Morphology-Controllable Fabrication of Sn-Sb Micro/Nano-Structures: Advanced Anode Materials for Lithium and Sodium Storage. *J. Power Sources* **2017**, *342*, 861−871.

(21) Lee, K. T.; Cho, J. Roles of Nanosize in Lithium Reactive Nanomaterials for Lithium Ion Batteries. *Nano Today* **2011**, *6*, 28−41.

(22) Zhang, Q.; Mao, J.; Pang, W. K.; Zheng, T.; Sencadas, V.; Chen, Y.; Liu, Y.; Guo, Z. Boosting the Potassium Storage Performance of Alloy-Based Anode Materials via Electrolyte Salt Chemistry. *Adv. Energy Mater.* **2018**, *8*, 1703288.

(23) Ding, H.; Wang, J.; Fan, L.; Liu, Z.; Jia, X.; Yu, X.; Lu, B. Sn-Sb Compounds with Novel Structure for Stable Potassium Storage. *Chem. Eng. J.* **2020**, *395*, 125147.

(24) Gabaudan, V.; Berthelot, R.; Sougrati, M. T.; Lippens, P.-E.; Monconduit, L.; Stievano, L. SnSbvs.Sn: improving the performance of Sn-based anodes for K-ion batteries by synergetic alloying with Sb. *J. Mater. Chem. A* **2019**, *7*, 15262−15270.

(25) Zhang, W.; Pang, W. K.; Sencadas, V.; Guo, Z. Understanding High-Energy-Density Sn_4P_3 Anodes for Potassium-Ion Batteries. *Joule* **2018**, *2*, 1534−1547.

(26) Zhang, W.; Mao, J.; Li, S.; Chen, Z.; Guo, Z. Phosphorus-Based Alloy Materials for Advanced Potassium-Ion Battery Anode. *J. Am. Chem. Soc.* **2017**, *139*, 3316−3319.

(27) Yin, D.; Chen, Z.; Zhang, M. Sn-Interspersed MoS_2/C Nanosheets with High Capacity for Na^+/K^+ Storage. *J. Phys. Chem. Solids* **2019**, *126*, 72−77.

(28) Huang, K.; Xing, Z.; Wang, L.; Wu, X.; Zhao, W.; Qi, X.; Wang, H.; Ju, Z. Direct Synthesis of 3D Hierarchically Porous Carbon/Sn Composites via in Situ Generated NaCl Crystals as Templates for Potassium-Ion Batteries Anode. *J. Mater. Chem. A* **2018**, *6*, 434−442.

(29) Fang, L.; Xu, J.; Sun, S.; Lin, B.; Guo, Q.; Luo, D.; Xia, H. Few-Layered Tin Sulfide Nanosheets Supported on Reduced Graphene Oxide as a High-Performance Anode for Potassium-Ion Batteries. *Small* **2019**, *15*, 1804806.

(30) Xing, L.; Yu, Q.; Bao, Y.; Chu, J.; Han, K.; Chong, S.; Lao, C.-Y.; Lai, F.; Li, P.; Xi, K.; Wang, W. Strong (001) Facet-Induced Growth of Multi-Hierarchical Tremella-Like Sn-Doped V_2O_5 for High-Performance Potassium-Ion Batteries. *J. Mater. Chem. A* **2019**, *7*, 25993−26001.

(31) Wang, G.; Aubin, M.; Mehta, A.; Tian, H.; Chang, J.; Kushima, A.; Sohn, Y.; Yang, Y. Stabilization of Sn Anode through Structural Reconstruction of a Cu-Sn Intermetallic Coating Layer. *Adv. Mater.* **2020**, *32*, 2003684.

(32) Xin, F.; Whittingham, M. S. Challenges and Development of Tin-Based Anode with High Volumetric Capacity for Li-Ion Batteries. *Electrochem. Energy Rev.* **2020**, *3*, 643−655.

(33) Sun, P.; Davis, J.; Cao, L.; Jiang, Z.; Cook, J. B.; Ning, H.; Liu, J.; Kim, S.; Fan, F.; Nuzzo, R. G.; Braun, P. V. High capacity 3D structured tin-based electroplated Li-ion battery anodes. *Energy Storage Mater.* **2019**, *17*, 151−156.

(34) Tian, H.; Li, Z.; Feng, G.; Yang, Z.; Fox, D.; Wang, M.; Zhou, H.; Zhai, L.; Kushima, A.; Du, Y.; Feng, Z.; Shan, X.; Yang, Y. Stable, high-performance, dendrite-free, seawater-based aqueous batteries. *Nat. Commun.* **2021**, *12*, 237.

(35) Zhang, Z.; Huang, Y.; Liu, X.; Wang, X.; Liu, P. Core-Shell Co, Zn Bimetallic Selenide Embedded Nitrogen-Doped Carbon Polyhedral Frameworks Assist in Sodium-Ion Battery Ultralong Cycle. *ACS Sustainable Chem. Eng.* **2020**, *8*, 8381−8390.

(36) Zhang, Z.; Huang, Y.; Liu, X.; Wang, X.; Liu, P. Yolk-shell structured $ZnCo_2O_4$ spheres anchored on reduced graphene oxide with enhance lithium/sodium storage performance. *Electrochim. Acta* **2020**, *342*, 136104.

(37) Zhang, Z.; Huang, Y.; Li, X.; Gao, X.; Liu, P.; Li, T. Rationally designed polyhedral carbon framework from solid to hollow for long cycle life secondary batteries. *J. Mater. Chem. A* **2021**, *9*, 6284−6297.

(38) Yang, L.; Dai, T.; Wang, Y.; Xie, D.; Narayan, R. L.; Li, J.; Ning, X. Chestnut-Like SnO_2/C Nanocomposites with Enhanced Lithium Ion Storage Properties. *Nano Energy* **2016**, *30*, 885−891.

(39) Yin, Y.; Rioux, R. M.; Erdonmez, C. K.; Hughes, S.; Somorjai, G. A.; Alivisatos, A. P. Formation of Hollow Nanocrystals Through the Nanoscale Kirkendall Effect. *Science* **2004**, *304*, 711−714.

(40) Cho, J. S.; Kang, Y. C. Nanofibers Comprising Yolk-Shell Sn@void@SnO/SnO_2 and Hollow SnO/SnO_2 and SnO_2 Nanospheres via the Kirkendall Diffusion Effect and Their Electrochemical Properties. *Small* **2015**, *11*, 4673−4681.

(41) Yang, Y.; Li, D.; Zhang, J.; Suo, G.; Yu, Q.; Feng, L.; Hou, X.; Ye, X.; Zhang, L.; Wang, W. Sn Nanoparticles Anchored on N Doped Porous Carbon as an Anode for Potassium Ion Batteries. *Mater. Lett.* **2019**, *256*, 126613.

(42) Shimizu, M.; Yatsuzuka, R.; Koya, T.; Yamakami, T.; Arai, S. Tin Oxides as a Negative Electrode Material for Potassium-Ion Batteries. *ACS Appl. Energy Mater.* **2018**, *1*, 6865−6870.

(43) Wang, H.; Xing, Z.; Hu, Z.; Zhang, Y.; Hu, Y.; Sun, Y.; Ju, Z.; Zhuang, Q. Sn-Based Submicron-Particles Encapsulated in Porous Reduced Graphene Oxide Network: Advanced Anodes for High-Rate

and Long Life Potassium-Ion Batteries. *Appl. Mater. Today* **2019**, *15*, 58−66.